Electrically Small Antenna For RFID-based Implantable Medical Sensor

Electrically Small Antenna For RFID-based Implantable Medical Sensor

Andrew J. Mugisha, Amin Rigi, Andreas Tsiamis, Symon Podilchak, Member, IEEE, and Srinjoy Mitra, Senior Member, IEEE

Scottish Microelectronics Centre, University of Edinburgh, Edinburgh EH9 3FF, UK

***Abstract*— We present a sub-GHz, low profile Electrically Small Antenna (ESA), designed for UHF RFID miniaturised battery free Implantable Wireless Medical Devices (IWMDs). The custom ESA is a linearly polarised dipole, and its topology leverages a meanderline structure to miniaturise its form factor. Furthermore, the ESA utilises a receded ground plane to improve its gain performance and achieve resonance, at the desired sub-GHz design frequency of 915 MHz. The ESA's dipole characteristics provide an added benefit of 180° bi-directional RF signal propagation. The ESA's design was optimised to integrate the footprint of a UHF RFID sensor chip (SL900A). By integrating the UHF RFID chip on the ESA, a complete wireless battery free sensory medical device, with an integrated antenna, can be realised. The antenna has a formfactor of 12.75×12.25×0.29 mm3. A prototype of the proposed ESA was fabricated and encapsulated in Polydimethylsiloxane (PDMS). Measurements of the prototyped ESA's input reflection coefficient (S11) and farfield gain values, at 915 MHz, were -26.44 dB and -18.88 dBi, respectively and demonstrated significantly better gain and efficiency performance, when compared to peer reviewed work. The ESA can be used as an antenna for various battery-free subcutaneous implants with a connected sensor (e.g. temperature) or actuator (e.g. neurostimulator).**

Index Terms*— *Electronically Small Antenna (ESA), linearly polarised antenna, Meanderline Patch Hybrid Dipole (MPHD), Implantable wireless medical device, Polydimethylsiloxane, Specific absorption rate.

I. Introduction

SOCIAL distancing and an increase in the demography with chronic illnesses have engendered a growth in demand for Implantable Wireless Medical Devices (IWMDs). As such, healthcare institutions are investing in smart wearable and implantable nodes for Wireless Body Area Networks (WBANs), to provide diagnostic, drug delivery and therapeutic medical services - remote healthcare services (RHS) [1]–[5]. For patient comfort and ease of clinical implementation, a miniature, subcutaneous IWMD with a low profile is a preferable implantable node. However, IWMDs present significant challenges with respect to the relationship between physical dimensions and wavelength.

Figure 1 shows the concept of a subcutaneously implanted PDMS encapsulated IWMD. The encapsulated IWMD could be implanted under the skin and interfaced with a wired deep-tissue sensor through an on-board Analog Front End (AFE) chip. A suitable transducer could also be fitted directly on the antenna PCB for a standalone subcutaneous IWMD.

The Encapsulated IWMD can be operated as a stand-alone device (a personal network), or as an integral node in a WBAN, linked to a cloud server through access points such as a mobile phone or Wi-Fi.

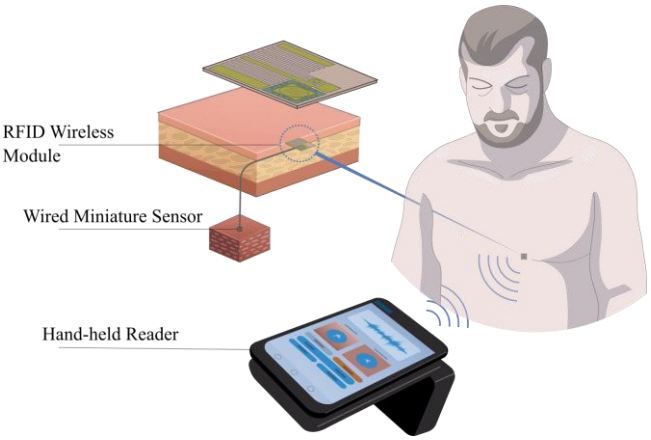

Fig. 1. Proposed antenna as part of a PDMS encapsulated Implantable Wireless Medical Devices (IWMD). The device is shown as a node in a wireless body area network (WBAN).

Most RFID systems generally provide the tag ID and possibly some basic data from an integrated sensor. However, some recent RFID chips include the possibility of connecting external sensors [6] which creates an opportunity of a battery-free RFID-based implantable sensor tag. Due to the size restriction of the antenna and absorption in body tissue, a UHF RFID is an ideal choice for such an application. SL900A[1] EPC Gen2 sensor tag (AMS, Austria) is one of these UHF RFID chips that has the capability of an external sensor interface.

A possible use case is shown in figure 1, where the RFID tag is implanted subcutaneously and connected to an external transducer implanted deeper in the body. Even with a 956MHz UHF band, the antenna volume must be significantly miniaturized for such a subcutaneous implant. Meanderline

[1] https://ams.com/en/sl900a

topologies have been widely implemented to address form factor miniaturisation, by compacting (bending) a physically long antenna element into a small structure. Best demonstrated, in [7] how to achieve a compact form factor, that resonated at low frequencies by implementing a meander topology. As the resonance frequency decreased, the antenna's radiation resistance also decreased. The resonance of an antenna shifts to higher frequencies, as the form factor decreases in physical size. As the antenna's largest dimension approaches $\lambda_0/10$ in length, its physical dimensions are electrically small, hence categorized as an electrically small antenna (ESA) [8].

UHF RFID systems have been widely researched for biomedical applications such as wearables gloves [9], textile substrate for wearable devices [10], remote temperature measurement for key workers and patients [11], [12]. RFID systems in the UHF band have shown high potential for implantable sensing applications in recent years. [13] has proposed a loop antenna and a Stacked Planar Inverted F Antenna reader antenna for a through the body human limb implant sensing applications. In [14] an implantable self-sensing UHF RFID loop dipole antenna was investigated. [15] has built a low-loss UHF RFID antenna for implanted dentures. Current UHF RFID systems have limitations for sensing application such as range and sensing accuracy, and the use of batteries are no desirable for implantable devices. In our previous work we improved the sensing performance both in range and accuracy by adding an energy harvesting module [12].

The UHF RFID ESA can be used for orthopedic implants, pacemakers, smart stents, neurostimulators and drug delivery electroceuticals. With minor modifications to the integrated footprint, the MPHD can be reconfigured for various RFID chipsets.

This paper investigates the design and simulation of the proposed antenna. Furthermore, looking into the characteristics of the fabricated antenna with and without PDMS encapsulation in free space and water.

II. FREE SPACE ESA DESIGN AND SIMULATIONS

A. ANTENNA DESIGN

Attributes of microstrip meanderline and patch elements were combined to realise the proposed antenna – a meanderline patch hybrid dipole (MPHD) topology. The meanderline elements and ground layer slotting (shrinking) are exploited, to realise an ESA that resonates at a sub-GHz frequency. The width of each patch element was varied, to achieve a finer tuning of the MPHD's resonance at the design frequency (f_0 = 915 MHz). Furthermore, the proposed antenna could operate as a subcutaneous repeater for deep implant wireless biosensors, by utilising the radiation pattern characteristics of a dipole. Figure 2 (A) is a CST model of the proposed PCB. The RFID chip is shown on bottom left and an empty space for a AFE chip is available on the bottom right.

The proposed antenna's physical dimensions are $12.75\times12.25\times0.29$ mm^3, $(0.039\lambda_0\times0.037\lambda_0\times0.887\text{e-}3\lambda_0)$. Where λ_0 is the free space wavelength, at the design frequency, f_0 = 915 MHz. The antenna's physical dimensions are significantly smaller than its free space wavelength ($\ll \lambda 0/10$). Hence, it can be classified as an ESA, as defined in [16]. The MPHD topology was realised on a Rogers RO4350 substrate, of height = 0.25 mm, with a dielectric constant ε_r = 3.66, and a loss tangent, tan δ = 0.0037 at 1 GHz, 23 °C. Annealed copper of thickness 18 μm was used to realise the conducting elements and on the ground layer. The annealed copper's skin depth was 2.2 μm.

At 915 MHz, a conventional halfwave dipole's length measures $\lambda_0/2$ = 163.82 mm. The meanderline structure was adopted, to conform (fit) a microstrip of significant length in a compact formfactor. Figure 2 (B) show the dimensions for the MPHD antenna element. When stretched at both ends, the proposed MPHD antenna's meanderline elements measures 105.07 mm (including the end patches). The thickness of the width of the meanderline is 0.23 mm.

Throughout this work, the elements of the MPHD model in figure 2(A), and the ground layer are optimised, to achieve the best performance. Simulation models and fabricated prototypes of the MPHD were evaluated in free space and water.

A comparison between the simulations and fabricated prototypes' results are presented. Furthermore, results are presented, for simulations of the MPHD, implanted in a 3-layer human tissue model. As a reference, a halfwave dipole was simulated in CST (f_0 = 915 MHz) and compared with the proposed MPHD model. The halfwave dipole's substrate was RO4350, of height 0.25 mm. The dimensions for the halfwave dipole model are $\lambda_0/2\times41\times0.25$ mm.

In figure 2(A), the model of a wireless chip was integrated onto the MPHD simulation model. The wireless sensory chip model was based on the $5\times5\times0.9$ mm^3 16-QFN epoxy package, for the SL900A ultra high frequency (UHF) radio frequency identification (RFID) chip, manufactured by Austria microsystems (AMS).

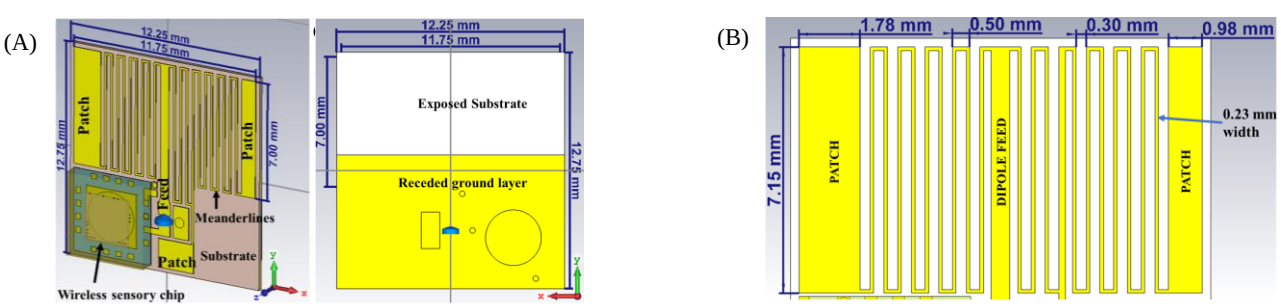

Fig. 2. (A) CST model of proposed antenna (Left) Meanderline patch hybrid dipole (MPHD) broadside, with wireless sensory chip model (Right) Ground plane with exposed substrate. On-board AFE can be placed on the bottom. **(B)** Dimensions of the MPHD antenna elements.

TABLE I
COMPARISON BETWEEN THE SIMULATED MPHD AND HALFWAVE DIPOLE MODEL AT 915 MHz

Topology	Dimensions (mm)	S_{11} (dB)	Gain (dBi)	η_{rad} (%)	R_{rad} (W)	R_{ohmic} (W)	10 dB BW (MHz)	Q
MPHD	12.75×12.25×0.29	-19.85	-21.09	0.78	53.61	3825.86	12	58.32
Halfwave dipole	163.82×41×0.29	-24.82	-1.7	27.93	46.9	121.01	22.3	31.38

B. NUMERICAL ANALYSIS

Table I compares key antenna parameters for the MPHD model vs the halfwave dipole model. The substrate height of each antenna is 0.25 mm plus 18 μm thick annealed copper on the broadside and ground layers, respectively. At resonance (915 MHz), the parameters S_{11}, antenna Gain and radiation efficiency (η_{rad}) were obtained from simulations in CST software. The MPHD has an antenna feed complex impedance, Z_{11}, = 52.63+*j*10.16 Ω. The radiation resistance (R_{rad}), the ohmic loss (R_{ohmic}), the 10 dB bandwidth, and the Q-factor were calculated using standard formulas. The MPHD's dimensions are 2.33% of the halfwave dipole. The respective MPHD's Gain is 0.95% that of the halfwave dipole. Hence, table I results indicate the importance of antenna size, particularly the importance of a sizable ground plane, in order to achieve decent antenna gain values. Based on the numerical analysis as the ohmic loss increases, the radiation efficiency decreases, thus degrading the antenna's gain.

The Q factor is inversely proportional to the antenna's bandwidth. Low profile miniaturised microstrip antennas tend to have high Q values, and as such very narrow bandwidth. This is particularly disadvantageous for narrowband antennas, when operated in a capacitively loaded medium, such as the human body. When implanted, the antenna's resonance shifts to a much lower frequency and is no longer centered at the targeted 10 dB bandwidth. Hence, at its feed, the antenna's reflection coefficient approaches unity. From the free space simulations, both the MPHD and halfwave dipole, have 10 dB BW frequency ranges which covers the UHF RFID upper band (908.94 - 920.94 MHz for the MPHD and 902.73 - 925.03 MHz for the halfwave dipole).

C. SIMULATION OF MPHD IN A BIOTISSUE MODEL

Human tissue consists of non-homogenous layers, primarily skin, fat, muscle and a high biofluid content.

Figure 3(A) shows a 3-layer human tissue model, used to simulate the performance of the MPHD in this work. A model was constructed, using parameters derived from extensive studies presented in [17]–[20], as follows:

- a 60×60×3 mm^2 top layer of skin, ε_r = 41.3,
- a 60×60×25 mm^2 mid-section layer of fat, $\varepsilon_r \approx 5.5$,
- and a 60×60×30 mm^2 bottom layer of muscle, $\varepsilon_r \approx 55$.

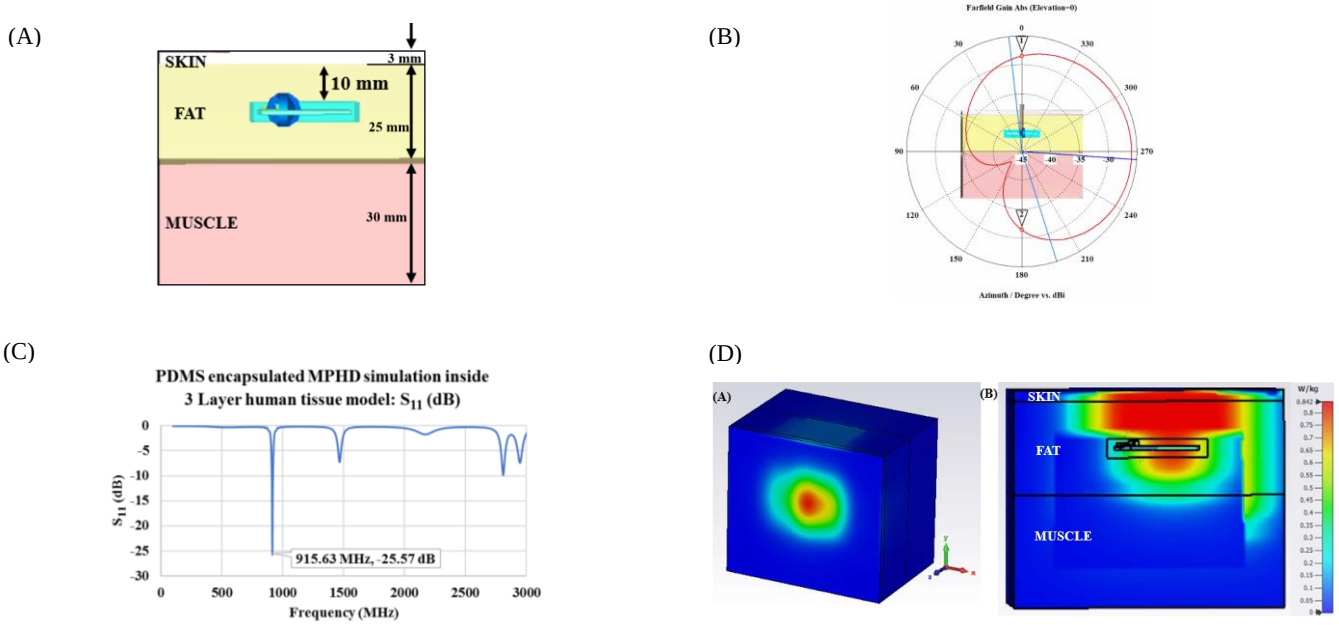

Fig. 3. (A) Cross-sectional view of the 3 Layer Human tissue model in CST, showing the implanted PDMS encapsulated MPHD in a 3-layer human tissue model. (B) Simulated 2D radiation plot, for the PDMS encapsulated MPHD inside the 3 Layer human tissue model in CST. (C) PDMS encapsulated MPHD S11 (dB) sweep. The MPHD was optimised to resonate at 915 MHz, inside a 3-layer human tissue model, at a 10 mm depth inside the fat layer. (D) SAR10g computation, inside the 3-layer human tissue model.

Simulations were performed, on the PDMS encapsulated MPHD, at an implant depth of 10 mm.

Figure 3(B) is a 2D radiation plot of the encapsulated MPHD inside the 3-layer human tissue model. At an elevation (El.) of 0°, azimuth (Az.) of ±180°, the respective simulated Gain values are -28.51 dBi (marker 1) and -31.44 dBi (marker 2). These Gain values are ≈ 10 dB lower than those for the PDMS encapsulated MPHD, when simulated in free space (figure 6(B)). Based on the 2D plots (figures 6(B) and 3(B)), the degradation in Gain can be attributed to the attenuative properties of the human tissue.

The PDMS encapsulated MPHD model was optimised inside the 3-layer human tissue model, to resonate at 915 MHz. Figure 3(C) shows the simulation results for a frequency sweep of the MPHD's S_{11}. At resonance, S_{11} = -25.57 dB.

Table II compares the -10 dB bandwidth of the PDMS encapsulated MPHD, simulated in free space, in a 3-layer human tissue model and in water.

The PDMS encapsulated MPHD's -10 dB bandwidth remains narrow, albeit increasing, slightly, as each medium's relative permittivity increases.

TABLE II
10 dB BANDWIDTH FOR PDMS ENCAPSULATED MPHD, IN 3 DIFFERENT MEDIA

Medium	**-10 dB BW (MHz)**
Free space	25.4
3-layer human tissue model	26.1
Water	28.2

SPECIFIC ABSORPTION RATE COMPUTATION

The International Commission on Non-Ionizing Radiation Protection (ICNIRP) guidelines recommend two methods for SAR computation [21]. The first being a stringent SAR_{1g} method, where the absorption level must not exceed 1.6 W/kg, averaged over a localised mass of 1 g of contiguous tissue. The second is the less stringent SAR_{10g} method, where the absorption level must not exceed 2.0 W/kg, averaged over a localised mass of 10 g of contiguous tissue. The recommended averaging time for localised SAR is 6 minutes, for the region of exposed mass, which absorbs the highest EM energy level.

CST uses the IEEE/IEC 62704-1-2017 FDTD method [22], to compute SAR. In the European union (EU), SAR_{10g} is the recommended metric for low power wireless devices, such as mobile phones. A UHF RFID reader, operating in the EU upper band must comply with the European telecommunications standard institute (ETSI) specification, which mandates an interrogator's maximum equivalent isotropic radiated power (EIRP) must not exceed +36 dBm (4 W) [23].

In compliance with the EU recommendations, SAR_{10g} computation was performed on the PDMS encapsulated MPHD, inside the 3-layer human tissue model. Figure 3(D) shows the SAR_{10g} computation model setup.

A peak SAR value of 0.842 W/kg was computed, at f_0 = 915 MHz. This value complies with the EU SAR_{10g} requirements, for the maximum allowable SAR level, due to exposure from a time varying EM source. The computed maximum allowable EM energy was based on an EIPR of 4 W source, to comply with the EU SAR_{10g} requirements.

III. CHARATRISATION OF FABRICATED MPHD ANTENNA IN FREE SPACE

A prototype of the MPHD antenna model in figure 2 was fabricated. The prototype was realised for operation in the 902 to 928 MHz UHF RFID upper band. Figure 4(C) is an illustration of the pre-assembled fabricated MPHD prototype. A footprint of the SL900A UHF RFID chip was realised on the antenna substrate's radiating broadside surface. The antenna's topology was realised by electroplating annealed copper of 18 µm thickness on the top and ground layers of an RO4350 substrate. The substrate height was 0.25 mm. Figure 4(C) shows an assembly of the MPHD, with a 3.5 mm RF Coax at the antenna feed. Two surface mount passive components (SMDs), used to implement a 50 Ω inverted L matching network topology, at the resonance frequency, f_0 = 915 MHz. In figure 4(C), the empty space, on the bottom right corner of the antenna's substrate can be mounted with a sensor interface (AFE: analog front-end) chip, used for pre-processing biosignals from external sensors. The processed biosignals can then be fed into the RFID chip, whose footprint is on the bottom left of the substrate. Data transferred from the pre-processing chip to the wireless sensory chip can then be transmitted to a remote access point. From the access point, the data can then be transmitted to a cloud medical server.

A. MPHD ANTENNA'S S_{11} AT RESONANCE

Figures 4(A) and 4(B) are the wideband and narrow band frequency plots for the MPHD's input reflection coefficient, S11, driven by a 50 Ω signal source.

The graphs show simulated results and the measured, (pre-matched and matched) S11 response over frequency. On the prototype, S11 was measured, using an 8753E Hewlett Packard vector network analyser (VNA). The pre-matched MPHD resonated at 912 MHz, with S_{11} = -20.62 dB (figure 4(B)). To achieve resonance at the design frequency, f_0 = 915 MHz, the MPHD's feed impedance was matched, transforming the impedance to $Z_{11} = 50.2\text{-}j10.75\ \Omega$ (S_{11} = -19.44 (dB)) at 915 MHz. An inverted L matching network topology, comprising of a series 6.8 pF 0402 capacitor and a shunt 12 nH 0402, to ground, was implemented at the MPHD's feed point as illustrated in figure 4(C). The matching network shifted the pre-match resonance, of the MPHD from 912 MHz to 915.63 MHz, as illustrated in figure 4(B).

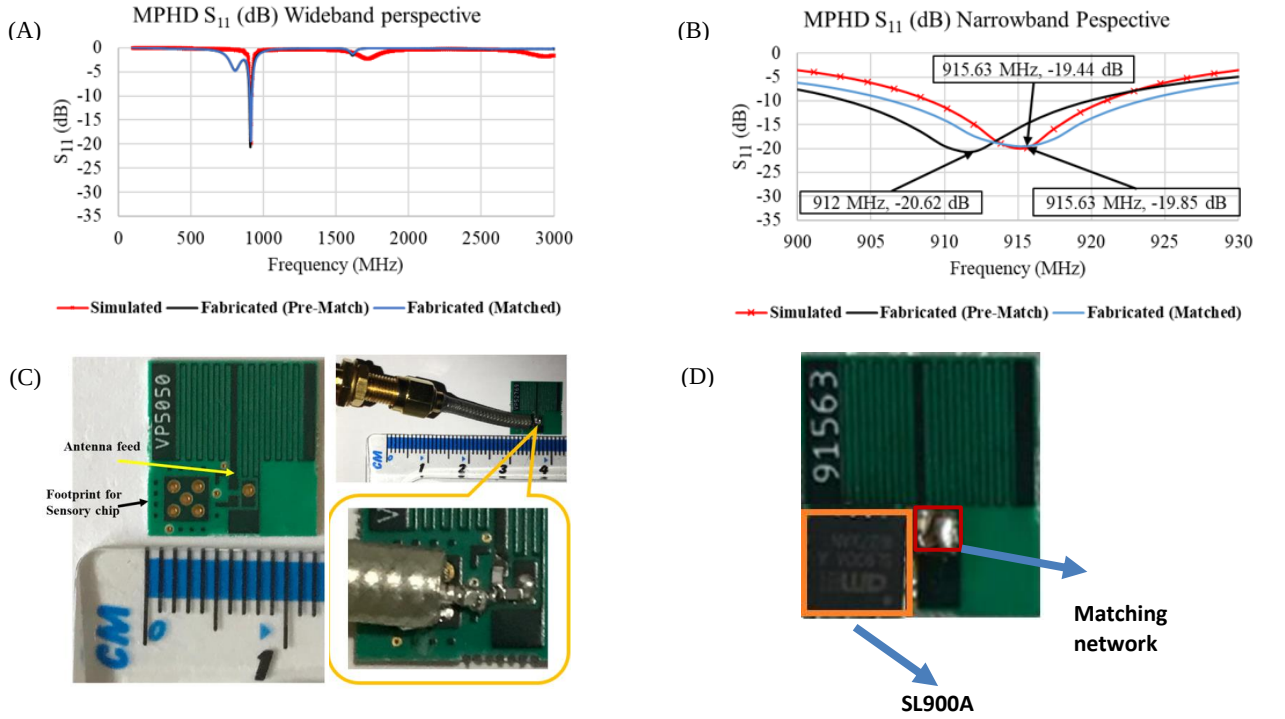

Fig. 4. (A) Wideband MPHD simulated and measured S11 frequency responses. (B) Narrowband MPHD simulated and measured S11 frequency responses (C) Left: MPHD prototype, pre-assembly. Right: 3.5 mm RF Coaxial, at antenna feed, with two SMD passive lumped elements used for matching the antenna to a 50 Ω load. (D) Fabricated antenna with SL900A chip and matching network.

The S_{11} measurements were performed in free space. The free space results are used as a reference (benchmark), prior to encapsulating the MPHD. Microstrip antennas which are encapsulated with a PDMS superstrate experience a shift in resonance to lower frequencies. While designing the antenna, it was anticipated that the superstrate would capacitively load the MPHD, and hence, shift its resonance to a lower frequency.

The MPHD has a narrow S_{11} 10 dB impedance bandwidth of ≈ 12.7 MHz (908.4 MHz to 921.1 MHz), which falls short of covering the ETSI UHF RFID upper band (902 MHz – 928 MHz). From equation (4), the prototype MPHD's quality factor was calculated, giving a Q = 55.06. The fabricated MPHD's measured 10 dB bandwidth and its calculated Q factor are comparable to those of the simulated results in table I. In this manuscript we primarily focus on characterising the ESA itself, but we integrated one prototype PCB with the SL900A chip to determine the validity of the entire system. The maximum working distance in direct line of sight in free space between the reader and the integrated prototype was 15cm after which the backscattered signal was no longer reliable or registered. The device under test included the SL900A chip and two component inverted L matching network between the chip and antenna. The antenna was matched to the SL900A antenna port impedance which is equal to 123+j300Ω, at 915 MHz. A beta layout UHF RFID reader was used in performing the RSSI measurements and the RSSI was -38 dBm. The reference antenna attached to the reader was a LAIRD 960 MHz, +9dBi linearly polarised antenna. The fully integrated system with antenna, SL900A sensory chip and matching network is shown in figure 4(D).

B. MPHD ANTENNA'S RADIATION PATTERNS

Figure 5(A) is a CST simulated 3D radiation plot showing electromagnetic (EM) energy, radiating from the MPHD. The EM energy propagates along the ±Z axis, with an E-field vector oriented in the x-y plane. From the plot in figure 5(A), the MPHD's simulated peak Gain value is -23.1 dBi, at 915 MHz. The 3D plot is typical of a linearly polarised dipole, radiating EM energy in diametrically opposite directions (±180°). This is advantageous for antennas which are used as repeaters.

Antenna Gain measurements were performed in an anechoic chamber, using a DAMS 7000 automated antenna measurement system [24]. Figure 5(C) shows images of the measurement test set up. A broad band (0.8 - 8 GHz) linearly polarised horn antenna was used as a reference. The reference antenna's Gain was +8 dBi at 915 MHz. The distance between the reference horn antenna and the MPHD was one meter.

A 2D radiation plot, comparing the simulated MPHD model's Gain vs the fabricated prototype's measured Gain, is shown in figure 5(B). The 2D plot represents a slice of the MPHD's EM radiation pattern at an elevation (El.) of 0° and swept through azimuth (Az.) of ± 180°, at 915 MHz. At Az. = 0°, the MPHD's simulated Gain, and measured Gain values were -23.04 dBi and -21.19 dBi, respectively. Likewise, at Az. = 180°, the MPHD's simulated, and measured Gain values were -22.96 dBi and -24.72 dBi, respectively. The slight tilt in the radiation pattern of the fabricated prototype's gain plot can be attributed to the measurement set up's long feed coax (figure 5(C)). The

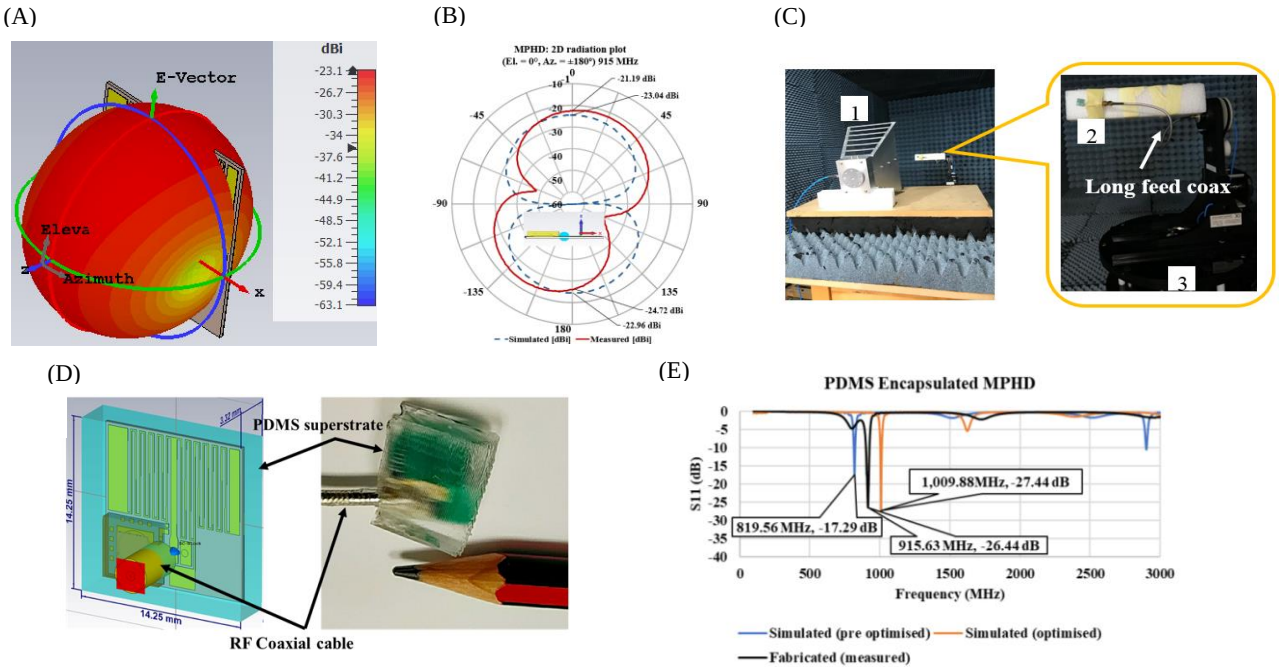

Fig. 5. (A) MPHD 3D radiation plot. (B) Simulated and measured 2D plots for MPHD at 915 MHz. (C) Gain measurement setup, in anechoic chamber. (1) is the reference horn antenna. (2) is the MPHD, and (3) is the DAMS 7000 rotary beam-stand. (D) PDMS encapsulated MPHD. (Left) Simulation model. (Right) Fabricated MPHD prototype in PDMS cast used for optimisation. (E) Encapsulated MPHD S11 plots

physical dimensions of the long feed coax physically extend the ground plane of the MPHD during measurement, hence capacitively loading the MPHD. Overall, the simulated and measured Gain results agree.

IV. ENCAPSULATED MPHD ANTENNA

Device encapsulation serves two key purposes: (i) insulation against biofouling of any electronic components, (ii) minimise the potential for immunorejection of the implant. Implantable devices are encapsulated, to ensure immunoisolation between the implant and biotissue. Bioencapsulation must also ensure patient comfort.

Polydimethylsiloxane (PDMS), a silicone based organic polymer, with material properties $\varepsilon_r = 2.5$, $tan\delta = 0.048$ at 1 GHz, was used to encapsulate the proposed antenna (figure 5(D)). The PDMS encapsulated MPHD formfactor measured $14.25 \times 14.25 \times 3.32\ mm^3$.

A. ENCAPSULATED MPHD S_{11} FREE SPACE RESPONSE

Free space simulations were performed on a PDMS encapsulated MPHD model, and its S_{11} results are shown in figure 5(E). The PDMS encapsulant capacitively loaded the MPHD model, shifting its resonance frequency to 819.563 MHz. As illustrated in figure 2, the MPHD model's elements and ground layer were optimised to correct the resonance offset introduced by the PDMS superstrate. The CST MPHD model was then optimised, shifting the resonance above f_0 by the difference between 915 MHz and 819.56 MHz (95.44 MHz). The new encapsulated MPHD CST model resonated at 1,009.88 MHz.

Based on the optimised MPHD model, a prototype was fabricated and encapsulated in PDMS. The prototype's feed complex impedance was matched to 50 Ω. At 915.63 MHz, the measured S_{11} = -26.44 dB (figure 15). This value is comparable to the simulated S_{11} = -27.43 dB, post optimisation (figure 11). Encapsulating the MPHD in PDMS changes the dielectric medium between the antenna and free space. Capacitively loading the MPHD with a PDMS encapsulant shifts the antenna's resonance to a lower frequency. To attain resonance at the desired frequency, f_0 = 915 MHz, the antenna elements of the MPHD in figure 2 were optimised. An inverted L matching network, of 2 SMD passive components, was implemented at the MPHD feed to improve S_{11}.

Figure 6(A) is a CST generated 3D radiation plot for the PDMS encapsulated MPHD model, showing a peak Gain value of -18.9 dBi, at 915 MHz. The MPHD is a dipole and thus radiates along the ±Z axis, a feature that can be beneficial for a device that is used as a repeater.

Gain measurements were performed on the PDMS encapsulated MPHD prototype (figure 5(D)), in an anechoic chamber, using the set up shown in figure 5(C). Results from the measurements were compared to simuation results, in figure 6(B). Figure 6(B) is a 2D radiation plot for the MPHD's simulated and measured Gain. The orientation of the MPHD under test was set at El. = 0°, relative to the reference horn antenna and swept through $\pm 180^{\circ}$ along the Az. axis. A comparison between the simulated and measured results is shown in figure 6(B).

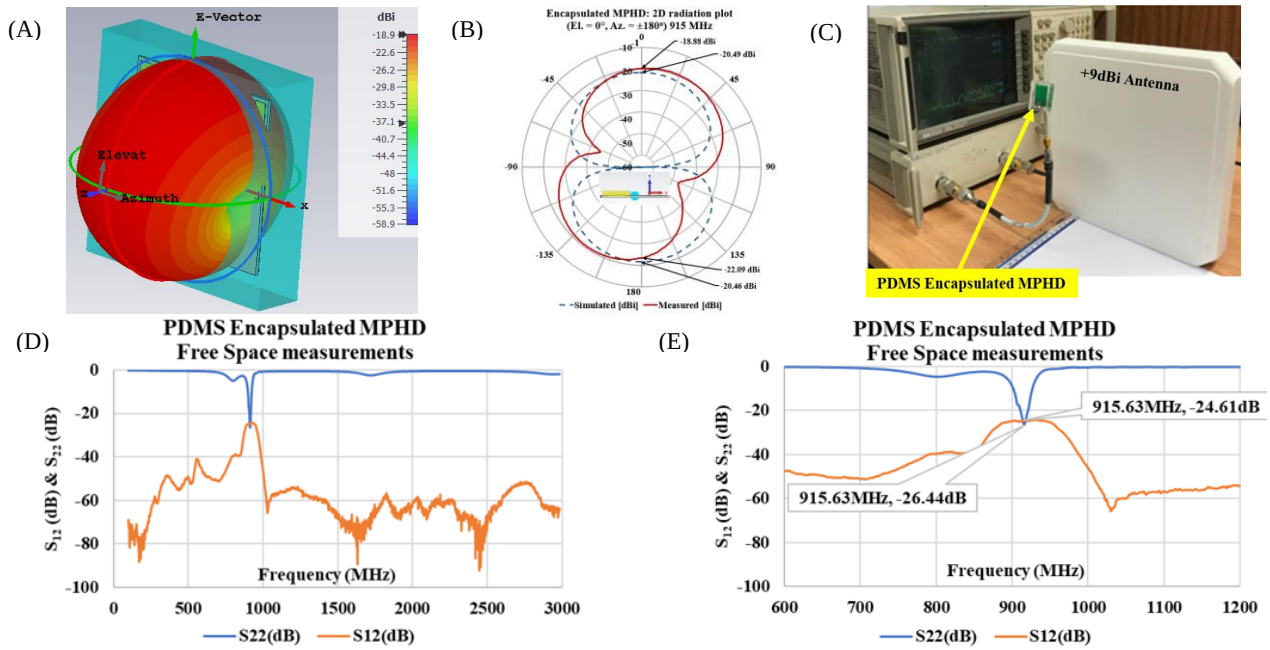

Fig. 6. (A) 3D radiation plot of the PDMS encapsulated in MPHD. (B) 2D radiation plot for PDMS encapsulated MPHD, for elevation at 0° and azimuth swept through 180°. (C) Setup for transmission loss (S12) and S22 measurements, on the PDMS encapsulated MPHD, in free space. (D) Wideband sweep S22 and S12 measurements performed on the encapsulated MPHD in free space. (E) Narrowband sweep S22 and S12 measurements performed on the encapsulated MPHD in free space.

At Az. = 0, the fabricated (and encapsulated) MPHD's Gain = -18.88 dBi. There was ≈ 2.3 dB improvement in Gain when compared with the prototype without encapsulation, at 915 MHz. Likewise, at Az. = 180°, the encapsulated MPHD's Gain improved by ≈ 2.6 dB.

B. TRANSMISSION LOSS IN FREE SPACE

Transmission loss is a key wireless link budget parameter. Using the FRIIS equation [25], transmission loss can be used to quantify the loss between a transmitting and receiving antenna. Reverse (S_{12}) and forward (S_{22}) transmission loss measurements were performed on the PDMS encapsulated MPHD, in a lab environment as shown in figure 6(D). The measurements were performed using an HP8753E vector network analyser (VNA). A commercial off the shelf (COTS) +9 dBi, linearly polarised antenna was used as a reference. The reference antenna's operating band is 902 to 928 MHz. Separation between the reference antenna and the MPHD was set at 3 cm. Figure 6(E) shows graphs for the reverse transmission loss (S12) and the reflection coefficient at the MPHD input (S22). At f_0 = 915 MHz, S12 = -24.61 dB, and S22 = -26.44 dB, measured over a separation distance of 3 cm (figure 7(A)). This is a distance over which a patient is expected to hold the reference antenna/reader unit from his/her body. These measurement results are used as a reference for subsequent measurements performed in water.

C. TRANSMISSION LOSS THROUGH WATER

Wireless implantable devices are designed to perform transcutaneous biotelemetry, through layers of bio-tissue. While accurate human body phantoms are rarely available, the results will be highly dependent with the site of implant (e.g., arm, abdomen, bony area), water is often used as the next best phantom. EM energy radiated by the MPHD must traverse media with a high-water content (non-homogenous human tissue layers). Water has a very high relative permittivity ($\varepsilon_r \approx 80$), and thus presents higher EM energy absorption/attenuation properties, compared to human/biotissue. Therefore, the performance of the MPHD is expected to degrade substantially, when characterized in a water only environment.

The simulated PDMS encapsulated MPHD model's elements were optimised to resonate at f_0 = 915 MHz, for a water medium. A prototype was fabricated and encapsulated, based on the simulation results. Transmission loss measurements were performed on the PDMS encapsulated MPHD prototype. Figure 7 shows the setup used to perform reverse transmission loss measurements (S_{12}), on the prototype, while immersed in a water filled Schott Fortuna II glass bowl. A spacing of 10

TABLE III
RESULTS FOR ENCAPSULATED MPHD T (S22) and (S12) SIMUALTED AND MEASURED IN WATER, f0 = 915 MHz.

Parameter	S_{12} (dB)	S_{22} (dB)
Measured	-42.13	-19.80
Simulated	-42.08	-33.81

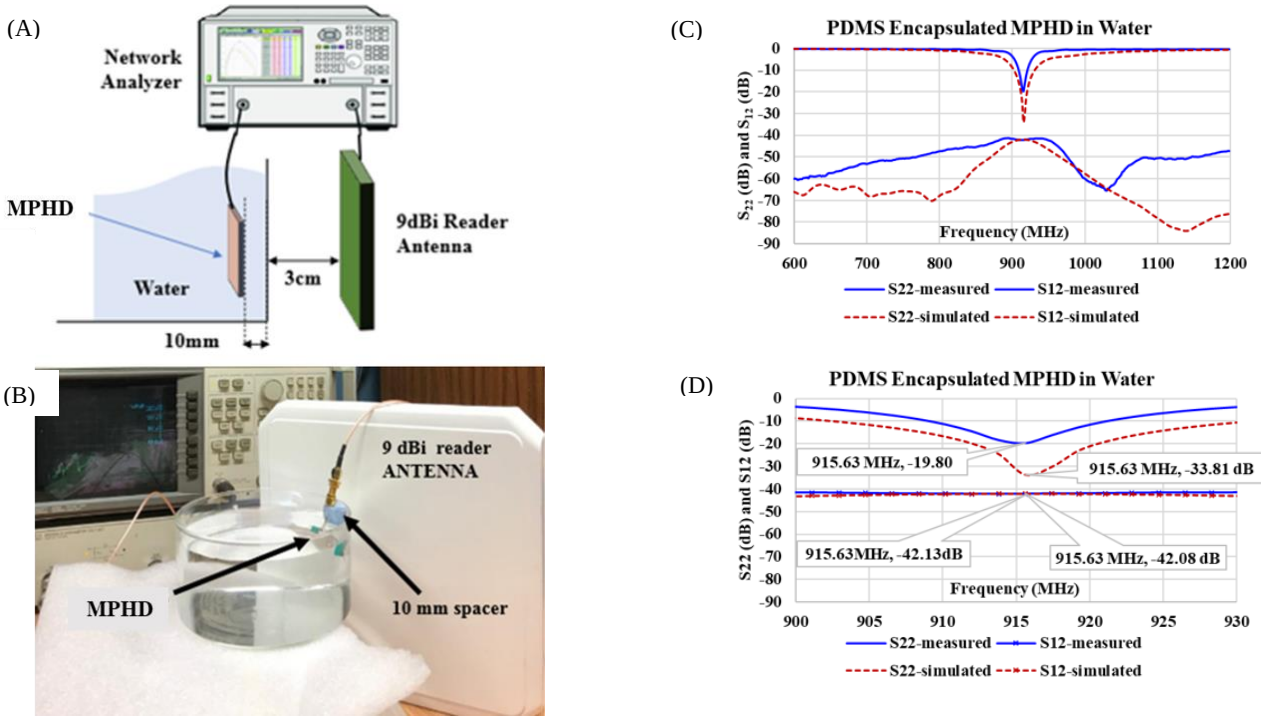

Fig. 7. (A) Setup for transmission loss measurements. MPHD is 10 mm inside water (10 mm from bowel wall). (A) Setup block diagram. (B) Lab setup. (C) Wideband sweep S22 and S12 measurements performed on the encapsulated MPHD in water. (D) Narrowband sweep S22 and S12 measurements performed on the encapsulated MPHD in water.

mm, between the Schott glass and the MPHD represents the device implantation depth (figure 7(B)).

Reverse transmission loss S_{12} and S_{22} measurements were performed on the encapsulated MPHD, in a water medium, using an HP8753E vector network analyser (VNA). Figures 7(C) and 7(D) show S_{12} and S_{22} measurement results in water. The reference antenna is positioned at Az. = 0°, and El. = 0°, relative to the MPHD.

The PDMS encapsulated MPHD prototype resonated at 915 MHz, with S22 ≈ -19.80 dB. Table III shows corresponding simulated and measured S12 and S22 results. At 915 MHz, the optimised, PDMS encapsulated MPHD prototype has a transmission loss of ≈ -42.13 dB when measured in water. At 3 cm, the transmission loss, between the PDMS encapsulated MPHD and the reference antenna, is degraded by ≈ 17.52 dB when measured in water, compared to the transmission loss measurements in free space.

V. COMPARISON WITH STATE OF THE ART IN-BODY ANTENNAS

Table IV is a compilation of eight 915 MHz implantable antennas, from recent publication, compared with the proposed MPHD. In table IV, only fabricated devices are presented. Each of the antennas in table V were characterised or tested inside a water medium or saline

TABLE IV
COMPARING PROPOSED MPHD TO OTHER FABRICATED 915 MHz IMPLANTABLE ANTENNAS.

Reference	Substrate	Dielectric constant (ε_r)	Dimensions (mm)	Vol. (mm^3)	S_{11} (dB)	Gain (dBi)	Depth (mm)
[26]	Flexible polyimide	2.25	$8.6^2 \times \pi \times 1$	232.35	No data	No Data	11.7
[27]	Rogers RO3010	10.2	11×11×1.27	153.67	No data	-29	4
[28]	Rogers RO3010	10.2	15×15×1.27	285.75	-14.5	-27	4
[29]	Rogers RO4003	3.38	$12.5^2 \times \pi \times 3$	1472.62	-12	-38	11
[30]	Rogers RT6010	10.2	8×6×0.5	24	-21	-28.5	4
[31]	Rogers RO3010	6.8	13.2x13.2x3.235	563.66	-21.78	-30.3	4
[32]	Rogers RO3010	4.3	32x10x0.025	8	-27.8	-28.7	-
[33]	Rogers RT6010	10.2	7x6x0.254	10.66	-25	-17.1	4
This work*	**Rogers RO4350**	**3.66**	**12.75×12.25×0.29**	**45.3**	**-26.44**	**-18.88**	**10**

* Measured parameters for MPHD in free space (figure 5). Dimensions are for the bare MPHD, without the PDMS encapsulant.

solution medium or skin mimicking phantom. However, the method of encapsulation is not described for any of these prototypes, hence we compare only the unencapsulated devices. The proposed system has one of the smallest volumes, a thin profile and one of the best S11 performance. Unlike all the other antennas, we also include the wireless RFID chip and the AFE chip footprint within the volume of the complete system. Among the devices measured around 10mm distance (a practical requirement for subcutaneous implants), the proposed solution has the best overall performance. The ESA can potentially be reconfigured to integrate other RFID chips and various Analog Front End Chips. Selection of the preferred material (RO4350) for the MPHD was based on a widely used low εr substrate for affordable, large volume, commercial printed circuit boards. Substrates with $\varepsilon r > 10$ have higher ohmic losses, at sub-GHz frequencies, and cost a premium.

VI. CONCLUSION

In this work, we propose an ESA for UHF RFID based implantable sensors. This is the only example of a UHF RFID system designed for an integrated sensor. The benefits of meanderline and slotted (receding) structures are exploited to miniaturise the formfactor of the antenna, designed to resonate at sub-GHz frequencies. The proposed antenna is designed as a reconfigurable platform, whose antenna elements can be optimised to resonate at a targeted design frequency in water, and human tissue. It has one of the best gain and frequency responses (S11), for subcutaneous implants. Along with a RFID sensor chip (e.g., SL900A), it can be connected to a deep implant sensor via an AFE and a wired transducer. The MPHD also provides a footprint for integrating a separate sensor interface chip (if necessary). To the best of our knowledge, the proposed device is the first implementation of an ESA for RFID-based implantable sensor with similar performance and form- factor.

REFERENCES

[1] M. Logambal, 'Healthcare Monitoring Systems: A WBAN Approach for Patient Monitoring', *International Journal on Future Revolution in Computer Science & Communication Engineering*, vol. 3, no. 12, pp. 26–31, Dec. 2017, [Online]. Available: shorturl.at/ciyKU

[2] I. Pandey, H. S. Dutta, and J. Sekhar Banerjee, 'WBAN: A Smart Approach to Next Generation e-healthcare System', in *2019 3rd International Conference on Computing Methodologies and Communication (ICCMC)*, Erode, India, Mar. 2019, pp. 344–349. doi: 10.1109/ICCMC.2019.8819713.

[3] P. K. D. Pramanik, A. Nayyar, and G. Pareek, 'WBAN: Driving e-healthcare Beyond Telemedicine to Remote Health Monitoring', in *Telemedicine Technologies*, Elsevier, 2019, pp. 89–119. doi: 10.1016/B978-0-12-816948-3.00007-6.

[4] A. K. Teshome, B. Kibret, and D. T. H. Lai, 'A Review of Implant Communication Technology in WBAN: Progress and Challenges', *IEEE Reviews in Biomedical Engineering*, vol. 12, pp. 88–99, 2019, doi: 10.1109/RBME.2018.2848228.

[5] S. A. Salehi, M. A. Razzaque, I. Tomeo-Reyes, and N. Hussain, 'IEEE 802.15.6 standard in wireless body area networks from a healthcare point of view', in *2016 22nd Asia-Pacific Conference on Communications (APCC)*, Yogyakarta, Indonesia, Aug. 2016, pp. 523–528. doi: 10.1109/APCC.2016.7581523.

[6] S. R. Khan, A. J. Mugisha, A. Tsiamis, and S. Mitra, 'Commercial Off-the-Shelf Components (COTS) in Realizing Miniature Implantable Wireless Medical Devices: A Review', *Sensors*, vol. 22, no. 10, Art. no. 10, Jan. 2022, doi: 10.3390/s22103635.

[7] S. R. Best, 'On the resonant properties of the Koch fractal and other wire monopole antennas', *IEEE Antennas and Wireless Propagation Letters*, vol. 1, pp. 74–76, 2002, doi: 10.1109/LAWP.2002.802550.

[8] N. K. Darimireddy, R. Ramana Reddy, and A. Mallikarjuna Prasad, 'Design of triple-layer double U-slot patch antenna for wireless applications', *Journal of Applied Research and Technology*, vol. 13, no. 5, pp. 526–534, Oct. 2015, doi: 10.1016/j.jart.2015.10.006.

[9] R. K. Singh, A. Michel, P. Nepa, and A. Salvatore, 'Wearable Dual-Band Quasi-Yagi Antenna for UHF-RFID and 2.4 GHz Applications', *IEEE Journal of Radio Frequency Identification*, vol. 4, no. 4, pp. 420–427, Dec. 2020, doi: 10.1109/JRFID.2020.3000298.

[10] D. Le, S. Ahmed, L. Ukkonen, and T. Björninen, 'A Small All-Corners-Truncated Circularly Polarized Microstrip Patch Antenna on Textile Substrate for Wearable Passive UHF RFID Tags', *IEEE Journal of Radio Frequency Identification*, vol. 5, no. 2, pp. 106–112, Jun. 2021, doi: 10.1109/JRFID.2021.3073457.

[11] A. J. Mugisha, A. Rigi, R. Joshi, A. Tsiamis, S. Podilchak, and S. Mitra, 'Towards a compact UHF RFID reader for wearable bio-sensing devices', in *2020 5th International Conference on Smart and Sustainable Technologies (SpliTech)*, 2020, pp. 1–6.

[12] A. Rigi, A. J. Mugisha, A. Arefian, S. R. Khan, and S. Mitra, 'Wireless Battery-Free Body Temperature Sensing Device for Key Workers', *IEEE Sensors Letters*, vol. 6, no. 2, pp. 1–4, Feb. 2022, doi: 10.1109/LSENS.2021.3131243.

[13] R. Lodato, V. Lopresto, R. Pinto, and G. Marrocco, 'Numerical and Experimental Characterization of Through-the-Body UHF-RFID Links for Passive Tags Implanted Into Human Limbs', *Antennas and Propagation, IEEE Transactions on*, vol. 62, pp. 5298–5306, Oct. 2014, doi: 10.1109/TAP.2014.2345586.

[14] V. Makarovaite, A. J. R. Hillier, S. J. Holder, C. W. Gourlay, and J. C. Batchelor, 'Passive UHF RFID Voice Prosthesis Mounted Sensor for Microbial Growth Detection', *IEEE Journal of Radio Frequency Identification*, vol. 4, no. 4, pp. 384–390, Dec. 2020, doi: 10.1109/JRFID.2020.3011900.

[15] J. Xu *et al.*, *Development of Denture Implanted RFID Tag Antennas*. 2018, p. 2. doi: 10.1109/iWEM.2018.8536610.

[16] K. Godeneli, U. Bengi, O. A. Kati, and S. Dumanli, 'A Wearable Dual-Mode Repeater Antenna for Implant Communications', *IEEE Transactions on Antennas and Propagation*, vol. 70, no. 2, pp. 868–875, Feb. 2022, doi: 10.1109/TAP.2021.3111603.

[17] N. Asan *et al.*, 'Characterization of the Fat Channel for Intra-Body Communication at R-Band Frequencies', *Sensors*, vol. 18, no. 9, p. 2752, Aug. 2018, doi: 10.3390/s18092752.

[18] G. C. R. Melia, 'Electromagnetic Absorption by the Human Body from 1 to 15 GHz', University of York, 2013. [Online]. Available: https://core.ac.uk/download/pdf/18451914.pdf

[19] I. Dove, 'Analysis of Radio Propagation Inside the Human Body for in-Body Localization Purposes', University of Twente, 2014. Accessed: Dec. 28, 2020. [Online]. Available: https://essay.utwente.nl/66071/1/Dove_MA_TE.pdf

[20] T. S. P. See, X. Qing, Z. N. Chen, C. K. Goh, and T. M. Chiam, 'RF transmission in/through the human body at 915 MHz', in *2010 IEEE Antennas and Propagation Society International Symposium*, Jul. 2010, pp. 1–4. doi: 10.1109/APS.2010.5561947.

[21] ICNIRP, 'GUIDELINES FOR LIMITING EXPOSURE TO ELECTROMAGNETIC FIELDS (100 kHz to 300 GHz) - 2020'. Health Phys. 118(5):483–524; 2020, Sep. 03, 2019. Accessed: Mar. 15, 2021. [Online]. Available: https://www.icnirp.org/cms/upload/publications/ICNIRPrfgdl2020.pdf

[22] 'IEC/IEEE International Standard – Determining the peak spatial-average specific absorption rate (SAR) in the human body from wireless communications devices, 30 MHz to 6 GHz - Part 1: General requirements for using the finite-difference time-domain (FDTD) method for SAR calculations', *IEC/IEEE 62704-1:2017*, pp. 1–86, Oct. 2017, doi: 10.1109/IEEESTD.2017.8088404.

[23] European Telecommunications Standards Institute, 'Radio Frequency Identification Equipment 865 MHz to 868 MHz up to 2W and 915 MHz up to 921 MHz up to 4 W.' European Telecommunications Standards Institute, 2018. [Online]. Available: https://www.etsi.org/deliver/etsi_en/302200_302299/302208/03.02.00_20/en_302208v030200a.pdf

[24] Diamond Engineering, 'DAMS 7000: Antenna automated measurement system'. Diamond Engineering, 2020. Accessed: Mar. 03, 2021. [Online]. Available: https://www.diamondeng.net/PDF/brochurelr.pdf

[25] J. A. Shaw, 'Radiometry and the Friis transmission equation', *American Journal of Physics*, vol. 81, no. 1, pp. 33–37, Jan. 2013, doi: 10.1119/1.4755780.

[26] L. Ukkonen, L. Sydanheimo, S. Ma, and T. Bjorninen, 'Backscattering-based wireless communication and power transfer to small biomedical implants', in *Microfluidics, BioMEMS, and Medical Microsystems XVIII*, San Francisco, United States, Feb. 2020, p. 9. doi: 10.1117/12.2552183.

[27] C. Liu, Y. Zhang, and X. Liu, 'Circularly Polarized Implantable Antenna for 915 MHz ISM-Band Far-Field Wireless Power Transmission', *Antennas Wirel. Propag. Lett.*, vol. 17, no. 3, pp. 373–376, Mar. 2018, doi: 10.1109/LAWP.2018.2790418.

[28] Y. Zhang, C. Liu, X. Liu, K. Zhang, and X. Yang, 'A Wideband Circularly Polarized Implantable Antenna for 915 MHz ISM-Band Biotelemetry Devices', *IEEE Antennas and Wireless Propagation Letters*, vol. 17, no. 8, pp. 1473–1477, Aug. 2018, doi: 10.1109/LAWP.2018.2849847.

[29] A. Sharma, E. Kampianakis, and M. S. Reynolds, 'A Dual-Band HF and UHF Antenna System for Implanted Neural Recording and Stimulation Devices', *Antennas Wirel. Propag. Lett.*, vol. 16, pp. 493–496, 2017, doi: 10.1109/LAWP.2016.2585650.

[30] S. A. A. Shah and H. Yoo, 'Scalp-Implantable Antenna Systems for Intracranial Pressure Monitoring', *IEEE Trans. Antennas Propagat.*, vol. 66, no. 4, pp. 2170–2173, Apr. 2018, doi: 10.1109/TAP.2018.2801346.

[31] S. Ahlawat *et al.*, 'Design and Performance Measurement of Implantable Differential Integrated Antenna for Wireless Biomedical Instrumentation Applications', *IEEE Transactions on Instrumentation and Measurement*, vol. 71, pp. 1–10, 2022, doi: 10.1109/TIM.2022.3185622.

[32] A. Basir, M. Zada, Y. Cho, and H. Yoo, 'A Dual-Circular-Polarized Endoscopic Antenna With Wideband Characteristics and Wireless Biotelemetric Link Characterization', *IEEE Transactions on Antennas and Propagation*, vol. 68, no. 10, pp. 6953–6963, Oct. 2020, doi: 10.1109/TAP.2020.2998874.

[33] M. Zada, I. A. Shah, and H. Yoo, 'Metamaterial-Loaded Compact High-Gain Dual-Band Circularly Polarized Implantable Antenna System for Multiple Biomedical Applications', *IEEE Trans. Antennas Propagat.*, vol. 68, no. 2, pp. 1140–1144, Feb. 2020, doi: 10.1109/TAP.2019.2938573.

ANDREW, J MUGISHA (M'20) received the BEng. (Hons) Electrical and Electronic Engineering, MSc. (eng.) from the University of Leeds (UK), and his Ph.D. from the University of Edinburgh (Nov '21). He worked at Nokia Ltd (UK), Motorola INC (USA), Sonyericsson INC (USA), Intel GmbH (Germany) as an RF Engineer, from 1998 until 2017. Currently he is working for AST-SpaceMobile. Andrew Mugisha was awarded the University of Edinburgh, School of Engineering Covid-19 Medal 2021 - Above and beyond contribution for the Development of a Wireless Battery-free Body Temperature Sensing for Constant Monitoring of Covid-19 Symptoms.

Amin Rigi received his BSc in Robotics Shahrood University of Technology, his MSc in Embedded Systems from Kingston University. He Further received an MSc in Sensors and Imaging systems from the University of Glasgow and The University of Edinburgh jointly. He is currently in his final year pursuing a PhD at the University of Edinburgh. Amin has been awarded more than 15 national and international awards for his research, some include first prize in the international biosensor competition (SensUs 2018), the University of Edinburgh Covid-19 Engineering Medal, a Scottish Edge award. His work has received international recognition and has been featured on the BBC, Discovery Channel, and Vice (Motherboard) to name a few.

Andreas Tsiamis received the B.Sc. degree in computer science, the B.Eng. degree in electronics and electrical engineering and the Ph.D. degree from The University of Edinburgh, U.K. In 2011, he joined the School of Engineering, The University of Edinburgh as a Post-Doctoral Researcher, where he is also a member of the Research Institute for Integrated Micro and Nano Systems. He has 15 years of experience on semiconductor research and development and has authored or co-authored more than 40 peer-reviewed journal papers and conference proceedings. His research has focused primarily on the design and fabrication of chemical and biomedical sensors and smart microsystems and in the development of More than Moore technologies. For his research he has developed novel semiconductor fabrication processes both at wafer and chip level. His present research focuses on field emitter array technology for medical imaging.

Symon K. Podilchak (S'03-M'05) received the B.A.Sc. degree in engineering science from the University of Toronto, Toronto, ON, Canada, in 2005, and the M.A.Sc. and Ph.D. degrees in electrical engineering from Queens University, Kingston, Canada, in 2008 and 2013, respectively. From 2013 to 2015, he was an Assistant Professor with Queens University. In 2015, he joined Heriot Watt University, Edinburgh, U.K., as an Assistant Professor, and became an Associate Professor in 2017. He is currently a Senior Lecturer with the School of Engineering, The University of Edinburgh, Edinburgh, Scotland. His research interests include surface waves, leaky-wave antennas, metasurfaces, UWB antennas, phased arrays, and RF integrated circuits.

SRINJOY MITRA (Senior Member, IEEE) received the M.Tech. degree from the Indian Institute of Technology, Bombay, India, and the Ph.D. degree from the Institute of Neuroinformatics (UNI), ETH Zurich, Switzerland. He was a Postdoctoral Researcher with Johns Hopkins University, Baltimore, MD, USA, before joining the Medical Electronics Team, IMEC, Belgium. He is currently a Senior Lecturer with the Institute for Integrated Micro and Nano Systems, The University of Edinburgh, U.K. His primary research interests include mixed-signal circuits and systems for sensor interfaces.